



Stability and dynamics of atom-molecule superfluids near a narrow Feshbach resonance

Zhiqiang Wang ^{1,2,3,4,*}, Ke Wang,¹ Zhendong Zhang,⁵ Shu Nagata,^{1,6} Cheng Chin,^{1,6} and K. Levin ¹

¹*Department of Physics and James Franck Institute, University of Chicago, Chicago, Illinois 60637, USA*

²*Hefei National Research Center for Physical Sciences at the Microscale and School of Physical Sciences, University of Science and Technology of China, Hefei, Anhui 230026, China*

³*Shanghai Research Center for Quantum Science and CAS Center for Excellence in Quantum Information and Quantum Physics, University of Science and Technology of China, Shanghai 201315, China*

⁴*Hefei National Laboratory, University of Science and Technology of China, Hefei 230088, China*

⁵*E. L. Ginzton Laboratory and Department of Applied Physics, Stanford University, Stanford, California 94305, USA*

⁶*Enrico Fermi Institute, University of Chicago, Chicago, Illinois 60637, USA*



(Received 9 October 2023; revised 13 June 2024; accepted 13 June 2024; published 11 July 2024)

The recent observations of a stable molecular condensate emerging from a condensate of bosonic atoms and related “super-chemical” dynamics have raised an intriguing set of questions. Here we provide a microscopic understanding of this unexpected stability and dynamics in atom-molecule superfluids; we show one essential element behind these phenomena is an extremely narrow Feshbach resonance in ^{133}Cs at 19.849G. Comparing theory and experiment, we demonstrate how this narrow resonance enables the dynamical creation of a large closed-channel molecular fraction superfluid, appearing in the vicinity of unitarity. Theoretically, the observed superchemistry (i.e., Bose-enhanced reactions of atoms and molecules) is found to be assisted by the formation of Cooper-like pairs of bosonic atoms that have opposite momenta. Importantly, this narrow resonance opens the possibility to explore the quantum critical point of a molecular Bose superfluid and related phenomena which would not be possible near a more typically broad Feshbach resonance.

DOI: [10.1103/PhysRevA.110.013306](https://doi.org/10.1103/PhysRevA.110.013306)

I. INTRODUCTION

Pairing in ultracold quantum gases and the preparation of quantum degenerate molecules have been long sought-after goals [1–3] for some time in the cold atom community. It provides access to new forms of many-body physics and quantum metrology. Historically, experiments in pursuit of such quantum degenerate ultracold molecules often have been hindered by cooling challenges and collisional loss [1,2,4]. That said, there have been successes, more numerous for fermionic systems [4–6]. Recently a stable $^{133}\text{Cs}_2$ molecular condensate consisting of bosonic ^{133}Cs atoms has been reported [7,8]. Here pairing interactions were induced in an atomic condensate based on a g -wave Feshbach resonance at $B_0 = 19.849(2)\text{G}$ [8].

In this article we show that essential for observing this molecular superfluid phase and a dynamically generated superchemistry [8] is a narrow Feshbach resonance used in the experiment to generate molecules [9]. This resonance of ^{133}Cs has a width $\Delta B = 8.3(5)\text{mG}$ [8], which is three to four orders of magnitude smaller than typically considered in ^7Li [10], ^{85}Rb [11,12], and ^{39}K [13,14]. See Table I (Here we use the dimensionless resonance-width parameter from the so-called many-body classification scheme [15].) This narrow resonance provides an explanation for the much wider stability regime and, importantly, enables access to the atom-molecule quantum critical point (QCP) [16,17] near the Feshbach resonance.

Through a comparison between theory and experiment, we demonstrate how a magnetic field quench, which sweeps an atomic superfluid to near unitarity, leads to a superfluid having a large closed-channel molecular fraction. Our theoretical analysis identifies an important role for out-of-equilibrium, noncondensed Cooper-like pairs, which are created by the Feshbach coupling during a transient stage. These are necessarily distinct from quantum depletion effects [18] that arise due to repulsive background scattering. We find the Feshbach-coupling-induced pairs fully participate in the coherent oscillations of the condensates that follow. That the associated oscillation frequency scales with the number of atoms reflects a coherent quantum chemical process stimulated by Bose enhancement, i.e., superchemistry [19–21].

The theoretical framework we employ incorporates a narrow Feshbach resonance and provides an integrated description of both the equilibrated system and the nonequilibrium dynamics. This narrow resonance ensures that the molecules near unitarity are predominantly closed-channel like, in contrast to the open-channel-dominated bound states studied previously [11,13,22–24]. The narrowness of the resonance, combined with a repulsive intermolecular interaction [7], leads to the unexpected stability at equilibrium [25–28].

To address this stability, we turn first to the theoretically calculated phase diagram depicted in Fig. 1. The figure shows that there are two superfluid phases: the atomic superfluid (ASF), in which both atomic and molecular condensates coexist, and the molecular superfluid (MSF), where the atomic condensate is missing [16,17]. We will return to this figure in

*Contact author: zqwang@uchicago.edu

TABLE I. Experimental parameters for Feshbach resonances in different Bose gases. In this table m_1 is the atomic mass, B_0 is the experimental resonance point, $\Delta\mu_m$ is the magnetic moment difference between a pair of atoms in the open channel and a molecule in the closed channel, ΔB is the resonance width in magnetic field, a_{bg} is the atom-atom background scattering length, and n is the experimental number density of atoms. In the last column, $x \equiv (k_n r_*)^{-1} = |k_n a_{\text{bg}}|^{-1} |\Delta\mu_m \Delta B| / E_{\text{bg}}$ is the dimensionless resonance-width parameter introduced in Ref. [15]. Here, $k_n = (6\pi^2 n)^{1/3}$ and $E_{\text{bg}} \equiv \hbar^2 / (m_1 a_{\text{bg}}^2)$. The data for ^{133}Cs , ^{85}Rb , and ^{39}K are collected from Refs. [7,8], Refs. [11,43], and Refs. [13,14], respectively. a_B is the Bohr radius, and μ_B is the Bohr magneton.

Atom	m_1 (atomic mass unit)	B_0	$\Delta\mu_m$	ΔB	a_{bg}	n	$x = (k_n r_*)^{-1}$
^{133}Cs	132.91	19.849 G	$0.57 \mu_B$	8.3 mG	$163 a_B$	$2.9 \times 10^{13} \text{ cm}^{-3}$	10^{-1}
^{85}Rb	84.91	155 G	$-2.23 \mu_B$	11.06 G	$-450 a_B$	$3.9 \times 10^{12} \text{ cm}^{-3}$	10^3
^{39}K	38.96	402.7 G	$1.5 \mu_B$	52 G	$-29 a_B$	$5.1 \times 10^{12} \text{ cm}^{-3}$	10^2

more detail later, but note a central conclusion: that there is only a narrow range of magnetic fields, mostly associated with the region between the so-called QCP and the zero crossing of the atomic scattering length, where instability is present.

Experimental background

Our experiments start with a Cs Bose-Einstein condensate (BEC) of 23 000 atoms at 22 nK in a pancakelike harmonic trap. The trap frequencies are $(\omega_x, \omega_y, \omega_z) = 2\pi \times (24, 13, 74)$ Hz. To initiate the nonequilibrium dynamics in the atomic and molecular channels, we quench the magnetic field to near the g -wave Feshbach resonance. After a variable evolution time, we decouple the atomic and molecular channels by quickly switching the magnetic field far below the resonance so that we can independently detect the population and temperature in each channel by focused time-of-flight (ToF) imaging. In this imaging molecules are first released into an isotropic harmonic trap for a quarter trap period before being dissociated above the Feshbach resonance. We also study molecule dissociation dynamics. For these latter experiments, we first

prepare a molecular condensate with a 23% BEC fraction [7,30]. Then the magnetic field is quenched close to the resonance and we monitor the atom number resulting from dissociation. For more details about the ToF imaging and experimental time line, see Appendix A.

II. THEORETICAL FRAMEWORK AND RESULTS

The narrowness of the resonance requires us to consider a theoretical framework associated with “two-channel” physics, in contrast to effective one-channel descriptions [31–39]. The Hamiltonian $\hat{H} = \hat{H}_1 + \hat{H}_2 + \hat{H}_3$ contains a kinetic energy (\hat{H}_1) for the two species (open-channel atoms and closed-channel molecules), the intraspecies repulsive interactions g_σ [7], and the Feshbach coupling α . Here,

$$\hat{H}_1 = \sum_{\mathbf{k}} \sum_{\sigma=1}^2 h_{\sigma\mathbf{k}} a_{\sigma\mathbf{k}}^\dagger a_{\sigma\mathbf{k}}, \quad (1a)$$

$$\hat{H}_2 = \frac{1}{V} \sum_{\mathbf{k}_i} \sum_{\sigma=1}^2 \frac{g_\sigma}{2} a_{\sigma\mathbf{k}_1}^\dagger a_{\sigma\mathbf{k}_2}^\dagger a_{\sigma, \mathbf{k}_3} a_{\sigma, \mathbf{k}_1 + \mathbf{k}_2 - \mathbf{k}_3}, \quad (1b)$$

$$\hat{H}_3 = -\frac{\alpha}{\sqrt{V}} \sum_{\mathbf{k}_i} (a_{1\mathbf{k}_1}^\dagger a_{1\mathbf{k}_2}^\dagger a_{2, \mathbf{k}_1 + \mathbf{k}_2} + \text{H.c.}). \quad (1c)$$

The subscripts $\sigma = 1$ and 2 represent open-channel atoms and closed-channel molecules, respectively. V is the volume, and $V^{-1} \sum_{\mathbf{k}} = \int^\Lambda d\mathbf{k} / (2\pi)^3$, where Λ is a cutoff, needed to regularize an ultraviolet divergence. We assume three-dimensional isotropy and ignore trap effects in our theory, as they do not affect qualitative conclusions.

In \hat{H}_1 , $h_{1\mathbf{k}} = (\hbar\mathbf{k})^2 / 2m_1 - \mu$ and $h_{2\mathbf{k}} = (\hbar\mathbf{k})^2 / 2m_2 - (2\mu - \nu)$, with $m_2 = 2m_1$, μ the chemical potential, and ν the bare-molecule state detuning. We distinguish ν from the detuning $\bar{\nu} \equiv \Delta\mu_m(B - B_0)$ through a B -independent constant; here, $\Delta\mu_m > 0$ is the difference in magnetic moments of the two channels, and B_0 is where the atomic two-body scattering length diverges, as in experiment. The eigenenergy of dressed molecules, denoted as ν_r in Fig. 1, is nearly equal to $\bar{\nu}$ for the g -wave resonance of ^{133}Cs at $B_0 = 19.849\text{G}$, except when $|B - B_0| \ll 1\text{mG}$ [9,29]. The α in \hat{H}_3 , given by $\alpha = \sqrt{(2\pi\hbar^2 a_{\text{bg}} / m_1) \Delta\mu_m \Delta B} / [1 - (2\pi) a_{\text{bg}} \Lambda]$ (see details in Appendix D), is chosen such that it reproduces the experimental resonance width ΔB in the two-body scattering limit.

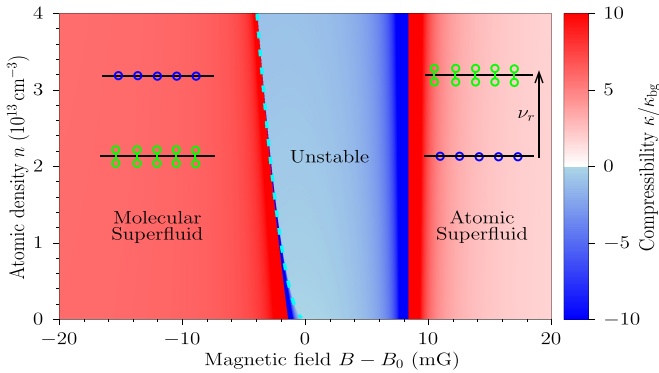


FIG. 1. Ground-state stability phases for the g -wave resonance of ^{133}Cs at $B_0 = 19.849\text{G}$ with width $\Delta B = 8.3\text{mG}$. Plotted is a map of the compressibility $\kappa = \partial n / \partial \mu$ as a function of atomic density n and magnetic field B , measured relative to B_0 . κ is normalized by $\kappa_{\text{bg}} = m_1 / (4\pi\hbar^2 a_{\text{bg}})$, with m_1 the atomic mass and a_{bg} the background scattering length. The atomic superfluid and molecular superfluid phases are stable in the red region, unstable in the blue. Indicated are the energy levels of atoms (blue circles) and molecules (green pairs), which characterize the phases with the molecular energy ν_r that is approximately $\propto (B - B_0)$ [29]. The dashed line (cyan) is the expected QCP, obtained without taking into account the stability issue.

TABLE II. Parameters used in the numerical simulation for ^{133}Cs . In this table, $k_n = (6\pi^2 n)^{1/3}$ and $E_n = \hbar^2 k_n^2 / 2m_1$ with $n = 2.9 \times 10^{13} \text{ cm}^{-3}$.

Λ	α	g_1	g_2
πk_n	$1.6 E_n / k_n^{3/2}$	$3.15 E_n / k_n^3$	$2.30 E_n / k_n^3$

To address *both* the statics and dynamics in a unified manner, we adopt a variational wave function,

$$|\Psi_{\text{var}}(t)\rangle = \frac{1}{\mathcal{N}(t)} e^{\sum_{\sigma=1}^2 \Psi_{\sigma 0}(t) \sqrt{V} a_{\sigma 0}^\dagger + \sum_{\mathbf{k}} \sum_{\sigma=1}^2 \chi_{\sigma \mathbf{k}}(t) a_{\sigma \mathbf{k}}^\dagger a_{\sigma-\mathbf{k}}^\dagger} |0\rangle.$$

In the exponent the \mathbf{k} sum is over half of \mathbf{k} space. $\Psi_{\sigma 0}$ and $\chi_{\sigma \mathbf{k}}$ are complex variational parameters, which are time-dependent (-independent) for our study of dynamics (statics). $|0\rangle$ is the vacuum that is annihilated by all $a_{\sigma \mathbf{k}}$. $\mathcal{N}(t)$ is the normalization factor. Here, in the spirit of generalized Bogoliubov theory, only pairwise correlations are included in the exponent of the variational wave function, which can be generally justified by the experimental observation [8] of undamped coherent oscillations of the populations which persist to long times.

The many-body dynamics associated with \hat{H} can be approximated through the variables $\Psi_{\sigma 0}(t)$ and $\chi_{\sigma \mathbf{k}}(t)$, which in turn are derived from the action [40–42] $\mathcal{S}[\Psi_{\sigma 0}^*(t), \Psi_{\sigma 0}(t), \chi_{\sigma \mathbf{k}}^*(t), \chi_{\sigma \mathbf{k}}(t)] = \int dt \langle \Psi_{\text{var}}(t) | (i\hbar \partial_t \Psi_{\text{var}}(t)) - \langle \Psi_{\text{var}}(t) | \hat{H} | \Psi_{\text{var}}(t) \rangle$. Minimizing \mathcal{S} with respect to $\{\Psi_{\sigma 0}^*, \Psi_{\sigma 0}, \chi_{\sigma \mathbf{k}}^*, \chi_{\sigma \mathbf{k}}\}$ leads to the following dynamical equations [30]:

$$i\hbar \frac{d}{dt} \Psi_{\sigma 0} = (h_{\sigma \mathbf{k}=0} + g_\sigma |\Psi_{\sigma 0}|^2 + 2g_\sigma n_\sigma) \Psi_{\sigma 0} + g_\sigma \Psi_{\sigma 0}^* x_\sigma - \delta_{\sigma,2} \alpha (x_1 + \Psi_{10}^2) - \delta_{\sigma,1} 2\alpha \Psi_{10}^* \Psi_{20}, \quad (2a)$$

$$i\hbar \frac{d}{dt} x_{\sigma \mathbf{k}} = 2[h_{\sigma \mathbf{k}} + 2g_\sigma (|\Psi_{\sigma 0}|^2 + n_\sigma)] x_{\sigma \mathbf{k}} + [g_\sigma (x_\sigma + \Psi_{\sigma 0}^2) - \delta_{\sigma,1} 2\alpha \Psi_{20}] (2n_{\sigma \mathbf{k}} + 1), \quad (2b)$$

where $\delta_{\sigma,\sigma'}$, with $\{\sigma, \sigma'\} = \{1, 2\}$, is the Kronecker delta. We relegate detailed derivations of these equations to Appendix C. In the above $\Psi_{\sigma 0} \equiv \langle a_{\sigma 0} \rangle / \sqrt{V}$, the ‘‘Cooper pair’’-like correlation [43] $x_{\sigma \mathbf{k}} \equiv \langle a_{\sigma \mathbf{k}} a_{\sigma-\mathbf{k}} \rangle = \chi_{\sigma \mathbf{k}} / (1 - |\chi_{\sigma \mathbf{k}}|^2)$, $n_{\sigma \mathbf{k}} \equiv \langle a_{\sigma \mathbf{k}}^\dagger a_{\sigma \mathbf{k}} \rangle = |\chi_{\sigma \mathbf{k}}|^2 / (1 - |\chi_{\sigma \mathbf{k}}|^2)$, $x_\sigma = V^{-1} \sum_{\mathbf{k} \neq 0} x_{\sigma \mathbf{k}}$, and $n_\sigma = V^{-1} \sum_{\mathbf{k} \neq 0} n_{\sigma \mathbf{k}}$. Here, $\langle \dots \rangle \equiv \langle \Psi_{\text{var}} | \dots | \Psi_{\text{var}} \rangle$. $x_{\sigma \mathbf{k}}$ is the expectation value of the (Cooper-like) pairing field for atoms or molecules. Note that both $x_{\sigma \mathbf{k}}$ and $n_{\sigma \mathbf{k}}$ are not independent. To obtain the dynamics we solve Eq. (2) together with the constraint $n = (|\Psi_{10}|^2 + n_1) + 2(|\Psi_{20}|^2 + n_2)$.

An advantage of working with the variational scheme is that the statics at equilibrium can be addressed simultaneously with the dynamics. At equilibrium, one minimizes the trial ground-state energy (\hat{H}) instead of \mathcal{S} with respect to the same set of variational variables, leading to a set of self-consistent conditions that are nearly identical to Eq. (2) except that the time derivatives in the latter are set to zero.

For all figures presented here, we use parameters for ^{133}Cs based on Refs. [7,8] (provided in Tables I and II), which have been chosen to reproduce the experimental resonance width ΔB and the atom-atom background scattering length a_{bg} . Knowing the density n , $k_n \equiv (6\pi^2 n)^{1/3}$, and $E_n =$

$\hbar^2 k_n^2 / (2m_1)$, we can calibrate the units of time in our dynamical calculations in terms of milliseconds (ms) and thus compare theory directly with experiment.

Solving the static version of Eq. (2) together with the number density constraint, we obtain the equilibrium values of $\Psi_{\sigma 0}$, x_σ , n_σ , μ , etc. as a function of both the detuning $\bar{\nu}$ and the total density n . To establish stability in the two-channel system, we numerically compute the compressibility $\kappa = \partial n / \partial \mu$.

Depending on whether κ is positive (stable) or negative (unstable), the phase diagram in Fig. 1 can be divided into three regimes: stable MSF phase, stable ASF phase, and an unstable regime near $\bar{\nu} = 0$. Stability in the MSF phase depends on an intermolecule repulsion, $g_2 > 0$. The stable MSF phase can persist to a regime well within the resonance width ΔB around unitarity, and just to the left of the presumed QCP. This is a unique and important characteristic of a narrow resonance as compared with a wide resonance. In the latter case the MSF-unstable phase boundary in Fig. 1 is pushed to the far left and is well separated from the QCP [44].

We turn next to our theoretical results for quenched dynamics, obtained from Eq. (2). We start with a pure atomic condensate, abruptly change the detuning to final values on either the positive or negative side of resonance, and then monitor the subsequent dynamical evolution of each component. The results presented in Fig. 2 show, after the quench, how the initially large atomic condensate contribution is quickly converted into a closed-channel molecular condensate (orange) as well as noncondensed pairs (blue). The most notable features are persistent oscillations in all components, seen for $B - B_0 \lesssim 1$ mG, which are most pronounced near unitarity. While the pairs and atomic condensate oscillate out of phase, the molecular condensate and pairs are nearly in phase. The pairs lead to very little dephasing on the molecular side, but above resonance for $B - B_0 \gtrsim 1$ mG, the oscillations are completely damped.

The calculation shows a substantial generation of atom pairs and molecules only within a narrow range of the Feshbach resonance. This can be understood as deriving from many-body entanglement generated in the dynamics, as near resonance the system is most strongly correlated. A quench can thus spread this entanglement over a larger portion of Hilbert space, thereby generating more correlated pairs and molecules near unitarity.

Also notable is an asymmetry (see also Appendix E) in the pair production between negative and positive detunings, which can be understood using the energy-level diagram of Fig. 1. For sweeps to the molecular side of resonance, energy conservation requires that the energy loss in a conversion from an atomic to molecular condensate be compensated by making more atom-pairs appear at higher energies.

Our results show rather good agreement with the following features of the experimental observations in Refs. [7,8]. We see a rapid relaxation toward a quasi-equilibrated phase where oscillations persist. These oscillations have a strong density dependence (associated with quantum ‘‘superchemistry’’), which will be addressed in more detail below. As will also be evident, the bulk of the closed-channel molecule production takes place over a relatively narrow range of fields roughly within the resonance width of $\Delta B \sim 8$ mG.

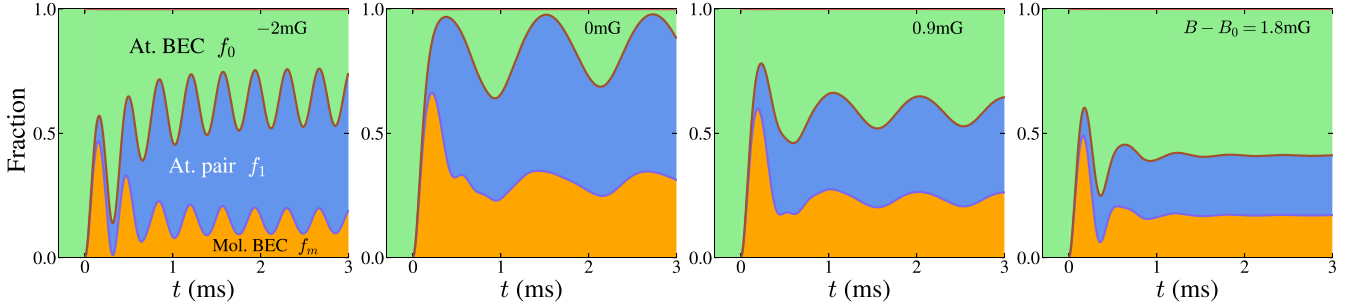


FIG. 2. Calculated coherent atom-molecule dynamics near resonance, obtained after a quench of a pure atomic condensate (at $t = 0$) to the four indicated magnetic fields $B - B_0$. Shown are atomic condensate fraction $f_0 = |\Psi_{10}|^2/n$ (green), atomic pair fraction $f_1 = n_1/n$ (blue), and molecular condensate fraction $f_m = 2|\Psi_{20}|^2/n$ (orange) vs time t . Noncondensed molecules are negligible. Here the total particle density is set to the experimental value of $n = 2.9 \times 10^{13} \text{cm}^{-3}$ [30].

III. COMPARISON BETWEEN THEORY AND EXPERIMENT

Specific plots illustrating the atomic and closed-channel molecule populations are presented in Figs. 3(a) and 3(b), respectively, with the top panels for theory and bottom for experiment. These are to be associated with the dynamics after a quench of an atomic condensate to different final detunings $\bar{\nu}$. We note that comparing curves with the “same” values of magnetic field in Fig. 3, a field recalibration might be considered, as we will see in Fig. 4(a) that there is a small offset in $B - B_0$ of the order of 2 mG between where the molecular fraction reaches a maximum in the theory as compared with experiment. One can also see from Fig. 3 that a more significant difference between theory and experiment is associated with the initial large overshoot, particularly of the molecular contribution, which is absent in the experiment. This

difference is likely due to inelastic particle-loss processes, which are most prevalent in the molecular channel. Another contributing factor to the difference is the fact that there is a non-negligible delay in transitioning the magnetic fields in the experiment, which can partially obscure or interfere with the early time measurements where the overshoot is observed in theory. At late times $t \gtrsim 1$ ms, the experimentally observed oscillations of atoms and molecules in Figs. 3(a) and 3(b) are not completely out of phase (see also Fig. 3(a) of Ref. [8]). This hints that there exists some small loss process that is coherent and persistent. Such a coherent loss process, which is absent in our theoretical simulations, will be investigated in future work.

The current narrow resonance of ^{133}Cs provides a unique opportunity to probe new issues which are not present in the moderately wide resonances typically used [11,13,22–24].

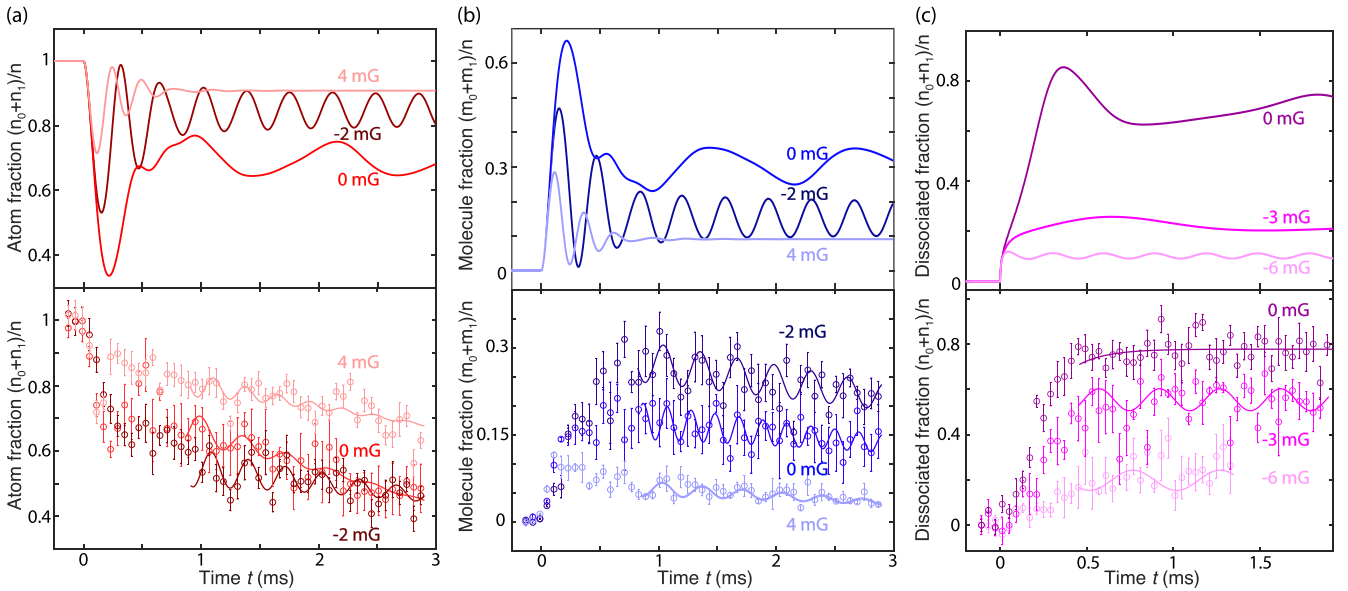


FIG. 3. Coherent atom-molecule dynamics, in theory (top panels) and experiment (bottom). Curves with the same color should be compared. Panels (a) and (b) respectively denote atomic and molecular channels, when an atomic condensate is quenched to different values of $B - B_0$ (in mG) near the resonance. $n_0 = |\Psi_{10}|^2$, $m_0 = 2|\Psi_{20}|^2$, $m_1 = 2n_2$. (For definitions of Ψ_{10} , Ψ_{20} , n_1 , and n_2 see text.) Plotted on the vertical axis in (c) is the fraction of molecules dissociated when a molecular condensate is quenched to different $B - B_0$ values. Solid lines (bottom panels) are fits to the data following the procedure in Ref. [8]; error bars represent one standard deviation from the mean. The particle density $n = 2.9 \times 10^{13} \text{cm}^{-3}$ [30].

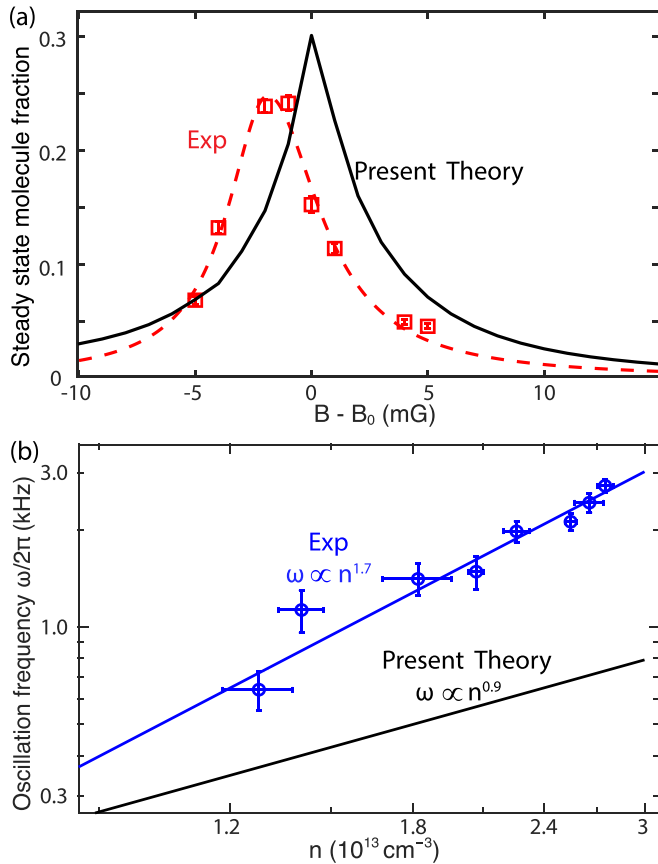


FIG. 4. (a) Closed-channel molecule fraction obtained as a time average after $t \approx 1$ ms [30], for the state reached after a quench as in Figs. 2, 3(a), and 3(b). The red open squares are experimental data for $n = 2.9 \times 10^{13} \text{ cm}^{-3}$; the red dashed line is a guide to the eye. (b) Density n dependence of the oscillation frequency ω near unity. The blue circles (with the blue line a power-law fit) are from previous experiments [8] compared with theory (black solid line).

In particular, we can consider the postquench dynamics for systems near unitarity, which are initially prepared as a molecular superfluid state. Theory predicts that the steady-state molecule dissociation fraction, reached after a transient stage, will increase with the final detuning $\bar{\nu}$ as $|\bar{\nu}| \rightarrow 0$. It is also interesting to note that a residual steady-state oscillation is observed in experiments which appears robustly in theory, provided a very small atomic condensate “seed” is introduced to the initial molecular superfluid state. Indeed, both these observations can be verified through a direct comparison between theory and experiment in Fig. 3(c), where the agreement is quite reasonable.

We turn to another comparison in Fig. 4(a) that addresses [45] the question at what range of magnetic fields, after a quench, is there an appreciable production of closed-channel molecules. Figure 4(a) plots the corresponding fraction, which is for the quasi-steady state associated with a time where the molecular fraction saturates, as in Figs. 3(a) and 3(b). From the figure one sees that in both theory and experiment, not only is the fraction largest in the near vicinity of resonance, but the maximum in both is between 20% and 30%. It is interesting to observe that this maximum closed-channel

molecular fraction (which has been a topic of interest both for dynamically generated [46] and equilibrated superfluids) is significantly lower than found for Fermi superfluids [47].

The phenomenon of “quantum superchemistry” [8,19–21] is of particular interest to explore, as it is reflected in a dependence of the oscillation frequency ω on the density n . Such a density dependence, indicative of a many-body Bose enhancement of chemical reactions, can be quantified as a power law $\omega \propto n^\gamma$ when $B = B_0$. Experiments find that $\gamma \approx 1.7$, while in the present theory $\gamma \approx 0.9$. Results from both theory and experiment are shown in Fig. 4(b) (see also Appendix F), although a more systematic comparison would require the inclusion of trap effects in the theory. Despite the fact that the exponents show some differences, what is important here is the observation of a Bose-enhanced chemistry even in the presence of Cooper-like pair excitations at finite momenta. While one might have expected these pairs to undermine or dissipate the oscillations, they appear to participate fully and maintain their coherence.

To interpret the superchemical oscillations, two phenomenological Hamiltonians, associated with two-body and three-body models, were used in Ref. [8], which contemplated only two modes, the atomic (Ψ_{10}) and molecular condensates (Ψ_{20}). We emphasize that even though the present two-channel Hamiltonian in Eq. (1) only contains Feshbach coupling and pairwise density-density interactions, it can induce the three-body processes discussed in Ref. [8]. These arise through scattering events that are of higher order than linear in the Feshbach coupling constant. This should not be surprising, since the Hamiltonian in Eq. (1) has been used in the literature [48] to discuss three-body recombination and related Efimov physics.

IV. CONCLUSIONS

In conclusion, in this paper we have shown that for the particular narrow g -wave Feshbach resonance at $B_0 = 19.849(2)\text{G}$ in ^{133}Cs the ground-state phase diagram around the predicted quantum critical point is interrupted only by a narrow region of instability. In the future one can study this QCP from the molecular side, which is in contrast to the situation for a typical “wide” resonance where this critical point is inaccessible [44].

We have also addressed the postquench dynamics around this resonance, primarily focusing on the coherent oscillations introduced by the quench. We have shown that for such an extremely narrow Feshbach resonance an appreciable fraction of closed-channel molecules can be produced from quenching an atomic BEC. Here, we provide comparisons between theory and experiment for the postquench dynamics, which involves three constituents that participate in the quasi-steady-state oscillations: two condensates along with correlated pairs of atoms. We caution that this paper is not focused on arriving at a precise quantitative agreement between theory and experiment, as various inelastic scattering processes such as three-body loss, atom-molecule, and molecule-molecule collisional losses are not included in the theoretical modeling. It is well known that these loss processes are extremely challenging to address for Bose gases near unitarity, in both theory and experiment.

Our work here emphasizes that the experimentally observed, quench-induced coherent oscillations [8] are consistent with the existence of noncondensed pairs, which importantly, do not undermine the highly collective nature of the observed superchemistry. This follows because the pairs participate fully along with both atom and molecule condensates in the coherent dynamics. In the future it will be interesting to look for more direct evidence of these pairs, using either pair-pair correlations as in Ref. [49] or matter-wave jet emissions as in Ref. [50].

We end by noting that our current studies of the g -wave resonance in ^{133}Cs , which provide an observation of a molecular BEC consisting of bosonic atoms, suggest an important role for our paper, as it serves to guide and encourage future efforts in other atomic gases with narrow resonances such as ^{23}Na [51], ^{87}Rb [52], ^{168}Er [53], where many of these same conclusions should apply.

ACKNOWLEDGMENTS

We thank Paul S Julienne, Qijin Chen, Zoe Yan, and Leo Radzihovsky for helpful discussions and communications at different stages of this project. This work is supported by the National Science Foundation under Grants No. PHY1511696 and No. PHY-2103542, and by the Air Force Office of Scientific Research under Award No. FA9550-21-1-0447. Z.Z. acknowledges support from a Grainger Graduate Fellowship and a Bloch Postdoctoral Fellowship, and S.N. acknowledges support from the Takenaka Scholarship Foundation. Z.W. is supported by the Innovation Program for Quantum Science and Technology (Grant No. 2021ZD0301904). We also acknowledge the University of Chicago's Research Computing Center for their support of this work.

APPENDIX A: PREPARATION AND DETECTION OF ATOMIC AND MOLECULAR BECS

The procedure to prepare a Cs BEC in the lowest hyperfine ground state at 19.5 G for the quench experiments shown in Figs. 3(a) and 3(b) is the same as that in Ref. [8], where atoms are in a pure optical trap without a magnetic field gradient for levitation. The atomic BECs have 23 000 atoms with a BEC fraction of 80%. We detect the remaining atoms after the quench dynamics by absorption imaging the atoms back at the off-resonant field value 19.5 G. We detect the created Cs_2 molecules, in the g -wave state $|f = 4, m_f = 4; \ell = 4, m_\ell = 2\rangle$, by first blowing away the remaining atoms using the atom imaging light pulse, releasing molecules into a weak horizontal harmonic trap with $\omega_x = \omega_y = 2\pi \times 15 \text{ Hz}$, and waiting for a quarter trap period $t_q = 17 \text{ ms}$. Finally, we image the molecules by jumping the field up to 20.4 G to dissociate them into atoms within 0.1 ms in the optical trap and then image the atoms from the dissociation [7,8]. We normalize both the atomic and molecular population by the initial total atom number during the quench dynamics as shown in Figs. 3(a) and 3(b). The missing fraction is due to various loss processes. We extract the asymptotic molecular fraction in the quasi-steady state, as presented in Fig. 4(a), by averaging data in the time window between 1 and 3 ms in the dynamics.

To create pure molecular samples used for the experiments shown in Fig. 3(c), we first make evaporatively cooled ultra-

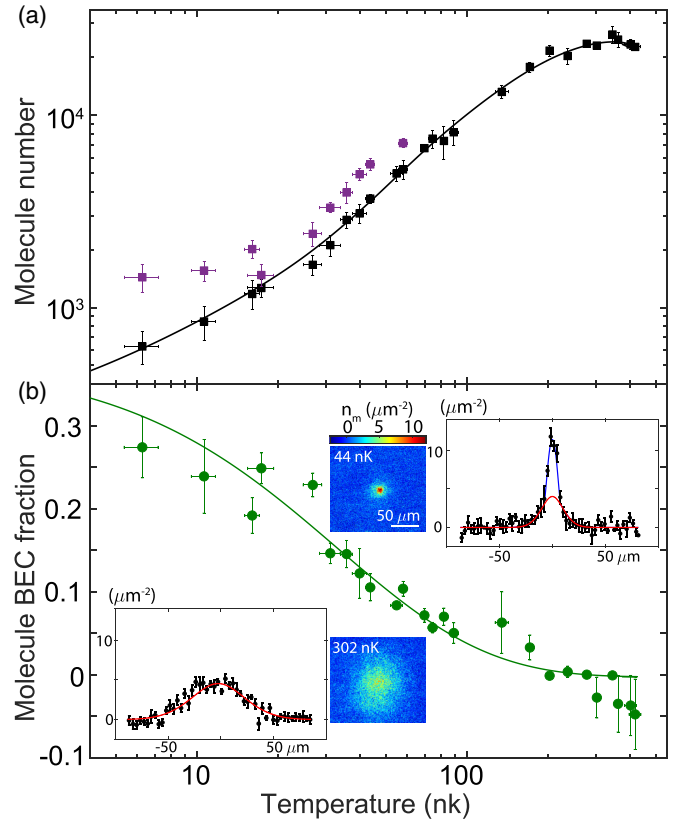


FIG. 5. Molecule number and molecular BEC fraction prepared at different temperatures. (a) Number of molecules created by associating atoms in ultracold atomic gases at different temperatures. The black (purple) data points are from 16.7 ms focused time-of-flight (ToF) (*in situ*) measurement. Lower detection efficiency in the ToF measurement is due to inelastic molecular collision-induced loss during the additional time of flight compared to the *in situ* imaging. (b) Molecular BEC fraction measured from the focused ToF imaging of the molecular density n_m , which shows bimodal distribution at sufficiently low temperature. The inset shows example images of molecules at 44 and 302 nK, respectively. The two panels next to the images show line cuts through the image centers, and the blue (red) solid lines represent BEC (thermal) components from a bimodal fit.

cold atomic gases at 20.22 G, where the magnetic field is calibrated *in situ* by atomic microwave spectroscopy. Then we switch to 19.89 G and ramp through the narrow g -wave Feshbach resonance to 19.83 G in 1.5 ms to associate atoms into molecules. After that, we quench the magnetic field to 19.5 G and apply a resonant light pulse to blow away the residual atoms. The resulting molecular temperature and population are characterized and shown in Fig. 5(a), where fewer and colder molecules are created from initial atomic gases at lower temperature and population. When the temperature is low enough, the molecular density after the focused time of flight starts to develop a bimodal distribution, from which we do fitting to extract the molecular BEC fraction [see Fig. 5(b)]. We choose to use molecular BECs at 27 nK with a BEC fraction of 23(1)% as the initial condition for the experiments shown in Fig. 3(c). After the magnetic field quench and a variable hold time, the atoms from molecule dissociation are imaged *in situ* for higher detection efficiency.

APPENDIX B: QUANTIFYING THE RESONANCE WIDTH

Early experiments on a bosonic Feshbach resonance by Donley and Claussen *et al.* [11,22] have focused on coherent oscillations between different Bose condensates below but near resonance. However, the Feshbach resonance employed, that of ^{85}Rb atoms at magnetic field $B_0 = 154.9\text{G}$, is very wide.

Using the many-body classification of resonance width in Ref. [15] [see Scheme (B) in their Eq. (4)], we estimate the dimensionless resonance-width parameter to be $x = (k_n r_*)^{-1} \sim 10^3 \gg 1$ for ^{85}Rb . For details, see Table I. Here, $k_n = (6\pi^2 n)^{1/3}$ with n the total atomic number density, and r_* is a length scale defined from the experimental resonance width. As a consequence of the extremely large x , the closed-channel molecular fraction near unitarity in these wide resonances is negligible [54]. In addition, the observed coherent oscillations in Refs. [11,22] are best interpreted as that between atomic

and ‘‘molecular’’-bound states, the latter of which are made up of open-channel atoms [35,39,54,55] and should be contrasted with the actual closed-channel molecules.

In contrast, the ^{133}Cs g -wave resonance used in Refs. [7,8] is extremely narrow. A simple estimate shows that $x \sim 0.1 \ll 1$, in agreement with the significant fraction of closed-channel molecules observed near unitarity in the experiments. The successful observation of molecules in this resonance not only enables us to explicitly study dissociation of molecular superfluids, but also provides us an opportunity to explore the role of the molecular superfluid component in postquench dynamics, starting with an initial state of open-channel (atomic) superfluid condensate. Theoretically, the inherent narrowness of the resonance requires us to consider a fully two-channel formulation in order to treat the dynamics adequately.

In Table I we present the relevant experimental parameters that we have used to estimate the resonance width for ^{133}Cs , ^{85}Rb , and ^{39}K .

APPENDIX C: DERIVATION OF EQ. (2) IN THE MAIN TEXT

In this section we give detailed derivations of Eq. (2) in the main text. We start with the time-dependent trial wave function [35],

$$|\Psi_{\text{var}}(t)\rangle = \frac{1}{\mathcal{N}(t)} \exp \left\{ \sum_{\sigma=1}^2 \Psi_{\sigma 0}(t) \sqrt{V} a_{\sigma \mathbf{k}=0}^\dagger + \sum'_{\mathbf{k} \neq 0} \sum_{\sigma=1}^2 \chi_{\sigma \mathbf{k}}(t) a_{\sigma \mathbf{k}}^\dagger a_{\sigma -\mathbf{k}}^\dagger \right\} |0\rangle, \quad (\text{C1})$$

where the prime sign in $\sum'_{\mathbf{k} \neq 0}$ indicates the sum is only over half momentum space such that each $\{\mathbf{k}, -\mathbf{k}\}$ pair is counted only once, where

$$\mathcal{N}(t) = \exp \left(\sum_{\sigma} |\Psi_{\sigma 0}(t)|^2 V/2 \right) \prod'_{\mathbf{k} \neq 0} \prod_{\sigma} (1 - |\chi_{\sigma \mathbf{k}}(t)|^2)^{-1/2} \quad (\text{C2})$$

is the normalization factor. In the exponent of Eq. (C1), $\Psi_{\sigma 0}$ and $\chi_{\sigma \mathbf{k}}$ are (complex) variational parameters, which are time-dependent for the study of dynamics. $\sum'_{\mathbf{k} \neq 0} = (1/2)V \int^{\Lambda} d\mathbf{k}/(2\pi)^3$, with V the volume and Λ a cutoff, needed to avoid ultraviolet divergence. $|0\rangle$ is the vacuum that is annihilated by all $a_{\sigma \mathbf{k}}$.

Assuming that the two-channel system, even when it is out of equilibrium, can be always approximated by $|\Psi_{\text{var}}(t)\rangle$, one maps the underlying quantum dynamics, described by the exact Heisenberg equation with the Hamiltonian \hat{H} , to that of a classical system. The latter is derived from the action [40–42]

$$\mathcal{S}[\Psi_{\sigma 0}^*(t), \Psi_{\sigma 0}(t), \chi_{\sigma \mathbf{k}}^*(t), \chi_{\sigma \mathbf{k}}(t)] = \int dt \{ \langle \Psi_{\text{var}}(t) | (i\hbar) \partial_t \Psi_{\text{var}}(t) \rangle - \langle \Psi_{\text{var}}(t) | \hat{H} | \Psi_{\text{var}}(t) \rangle \} \quad (\text{C3})$$

$$\equiv \int dt L[\Psi_{\sigma 0}^*(t), \Psi_{\sigma 0}(t), \chi_{\sigma \mathbf{k}}^*(t), \chi_{\sigma \mathbf{k}}(t)]. \quad (\text{C4})$$

Using $\Psi_{\text{var}}(t)$ and the Hamiltonian in Eq. (1) of the main text, we evaluate the two terms on the right-hand side of Eq. (C3) as follows (for brevity we suppress all the time dependences in the following):

$$\langle \Psi_{\text{var}} | (i\hbar) \partial_t \Psi_{\text{var}} \rangle = \sqrt{V} \sum_{\sigma} \left[(i\hbar) \frac{d}{dt} \Psi_{\sigma 0} \right] \langle a_{\sigma \mathbf{k}=0}^\dagger \rangle + \sum'_{\mathbf{k} \neq 0} \sum_{\sigma} \left[(i\hbar) \frac{d}{dt} \chi_{\sigma \mathbf{k}} \right] \langle a_{\sigma \mathbf{k}}^\dagger a_{\sigma -\mathbf{k}}^\dagger \rangle + (i\hbar) \frac{d}{dt} \ln \mathcal{N}^{-1}, \quad (\text{C5})$$

$$= V \sum_{\sigma} \frac{i\hbar}{2} \left(\Psi_{\sigma 0}^* \frac{d}{dt} \Psi_{\sigma 0} - \Psi_{\sigma 0} \frac{d}{dt} \Psi_{\sigma 0}^* \right) + \sum'_{\mathbf{k} \neq 0} \sum_{\sigma} \frac{1}{1 - |\chi_{\sigma \mathbf{k}}|^2} \frac{i\hbar}{2} \left(\chi_{\sigma \mathbf{k}}^* \frac{d}{dt} \chi_{\sigma \mathbf{k}} - \chi_{\sigma \mathbf{k}} \frac{d}{dt} \chi_{\sigma \mathbf{k}}^* \right), \quad (\text{C6})$$

where we have introduced the shorthand notation $\langle \dots \rangle \equiv \langle \Psi_{\text{var}} | \dots | \Psi_{\text{var}} \rangle$. The other term on the right-hand side of Eq. (C3) is given by

$$\begin{aligned} \langle \Psi_{\text{var}} | \hat{H} | \Psi_{\text{var}} \rangle &= h_{\sigma \mathbf{k}=0} V |\Psi_{\sigma 0}|^2 + \frac{g_{\sigma}}{2} V |\Psi_{\sigma 0}|^4 - \alpha V ((\Psi_{\sigma 0}^*)^2 \Psi_{20} + \text{c.c.}) + \sum_{\mathbf{k} \neq 0} \sum_{\sigma} (h_{\sigma \mathbf{k}} + 2g_{\sigma} |\Psi_{\sigma 0}|^2 + g_{\sigma} n_{\sigma}) n_{\sigma \mathbf{k}} \\ &+ \sum_{\mathbf{k} \neq 0} \sum_{\sigma} \frac{g_{\sigma}}{2} ((\Psi_{\sigma 0}^*)^2 \chi_{\sigma \mathbf{k}} + \text{c.c.}) + \sum_{\sigma} \frac{g_{\sigma}}{2} V |x|^2 - \alpha \sum_{\mathbf{k} \neq 0} (\Psi_{20} x_{1\mathbf{k}}^* + \text{c.c.}). \end{aligned} \quad (\text{C7})$$

In arriving at Eqs. (C6) and (C7), we have used

$$\Psi_{\sigma 0} \equiv \langle a_{\sigma 0} \rangle / \sqrt{V}, \quad (\text{C8a})$$

$$x_{\sigma \mathbf{k}} \equiv \langle a_{\sigma \mathbf{k}} a_{\sigma -\mathbf{k}} \rangle = \chi_{\sigma \mathbf{k}} / (1 - |\chi_{\sigma \mathbf{k}}|^2), \quad (\text{C8b})$$

$$n_{\sigma \mathbf{k}} \equiv \langle a_{\sigma \mathbf{k}}^\dagger a_{\sigma \mathbf{k}} \rangle = |\chi_{\sigma \mathbf{k}}|^2 / (1 - |\chi_{\sigma \mathbf{k}}|^2), \quad (\text{C8c})$$

$$x_\sigma = V^{-1} \sum_{\mathbf{k} \neq 0} x_{\sigma \mathbf{k}}, \quad n_\sigma = V^{-1} \sum_{\mathbf{k} \neq 0} n_{\sigma \mathbf{k}}. \quad (\text{C8d})$$

$x_{\sigma \mathbf{k}}$ is the expectation value of the (Cooper-like) pairing field for atoms ($\sigma = 1$) or molecules ($\sigma = 2$).

Minimizing \mathcal{S} with respect to $\{\Psi_{\sigma 0}^*, \chi_{\sigma \mathbf{k}}^*\}$ leads to the following Euler-Lagrange equations:

$$\frac{\partial L}{\partial \Psi_{\sigma 0}^*} - \frac{d}{dt} \frac{\partial L}{\partial (\partial_t \Psi_{\sigma 0}^*)} = 0 \quad (\text{C9})$$

$$i\hbar \frac{d}{dt} \Psi_{10} = (h_{1\mathbf{k}=0} + g_1 |\Psi_{10}|^2 + 2g_1 n_1) \Psi_{10} + g_1 \Psi_{10}^* x_1 - 2\alpha \Psi_{10}^* \Psi_{20}, \quad (\text{C15a})$$

$$i\hbar \frac{d}{dt} \Psi_{20} = (h_{2\mathbf{k}=0} + g_2 |\Psi_{20}|^2 + 2g_2 n_2) \Psi_{20} + g_2 \Psi_{20}^* x_2 - \alpha (x_1 + \Psi_{10}^2), \quad (\text{C15b})$$

$$i\hbar \frac{d}{dt} x_{1\mathbf{k}} = 2[h_{1\mathbf{k}} + 2g_1 (|\Psi_{10}|^2 + n_1)] x_{1\mathbf{k}} + [g_1 (x_1 + \Psi_{10}^2) - 2\alpha \Psi_{20}] (2n_{1\mathbf{k}} + 1), \quad (\text{C15c})$$

$$i\hbar \frac{d}{dt} x_{2\mathbf{k}} = 2[h_{2\mathbf{k}} + 2g_2 (|\Psi_{20}|^2 + n_2)] x_{2\mathbf{k}} + g_2 (x_2 + \Psi_{20}^2) (2n_{2\mathbf{k}} + 1). \quad (\text{C15d})$$

We emphasize that in evaluating the partial derivative, $\partial \langle \hat{H} \rangle / \partial \chi_{\sigma \mathbf{k}}^*$, to obtain the last two equations, we have to include contributions from terms in $\langle \hat{H} \rangle$ [Eq. (C7)], both at \mathbf{k} and $-\mathbf{k}$, as each $\{\mathbf{k}, -\mathbf{k}\}$ pair shares the same variational parameter $\chi_{\sigma \mathbf{k}}$ in the exponent of our variational wave function [see Eq. (C1)]. Otherwise, the $dx_{\sigma \mathbf{k}}/dt$ obtained will differ from the above expressions by a factor of 2.

An alternative derivation

In this section we sketch an alternative derivation for Eq. (C15), which shows more explicitly in what sense the quantum dynamics can be mapped to the classical-dynamics described by the action \mathcal{S} in Eq. (C3). It may also help us to better understand when the classical equations derived from \mathcal{S} will become inadequate in future applications, although such a potential breakdown is not of the major concern to our current paper.

In this alternative approach, we start with the exact Heisenberg equation for a generic operator $\hat{O}(t) \equiv e^{i\hat{H}t/\hbar} \hat{O} e^{-i\hat{H}t/\hbar}$:

$$\frac{d\hat{O}(t)}{dt} = \frac{i}{\hbar} [\hat{H}, \hat{O}(t)]. \quad (\text{C16})$$

Within our current variational wave-function scheme, \hat{O} can be either $a_{\sigma \mathbf{k}=0}$ or $a_{\sigma \mathbf{k}} a_{\sigma -\mathbf{k}}$. Next, we make the following central approximation:

$$\frac{d}{dt} \langle \hat{O}(t) \rangle \approx \left\langle \frac{d\hat{O}(t)}{dt} \right\rangle = \frac{i}{\hbar} \langle [\hat{H}, \hat{O}(t)] \rangle. \quad (\text{C17})$$

$$\Rightarrow V(i\hbar) \frac{d}{dt} \Psi_{\sigma 0} = \frac{\partial}{\partial \Psi_{\sigma 0}^*} \langle \hat{H} \rangle, \quad (\text{C10})$$

$$\frac{\partial L}{\partial \chi_{\sigma \mathbf{k}}^*} - \frac{d}{dt} \frac{\partial L}{\partial (\partial_t \chi_{\sigma \mathbf{k}}^*)} = 0 \quad (\text{C11})$$

$$\Rightarrow \frac{1}{(1 - |\chi_{\sigma \mathbf{k}}|^2)^2} (i\hbar) \frac{d}{dt} \chi_{\sigma \mathbf{k}} = \frac{\partial}{\partial \chi_{\sigma \mathbf{k}}^*} \langle \hat{H} \rangle. \quad (\text{C12})$$

From Eq. (C12) and its complex conjugate, we then derive

$$i\hbar \frac{d}{dt} x_{\sigma \mathbf{k}} = \frac{i\hbar}{(1 - |\chi_{\sigma \mathbf{k}}|^2)^2} \left(\frac{d\chi_{\sigma \mathbf{k}}}{dt} + \chi_{\sigma \mathbf{k}}^2 \frac{d\chi_{\sigma \mathbf{k}}^*}{dt} \right) \quad (\text{C13})$$

$$= \frac{\partial}{\partial \chi_{\sigma \mathbf{k}}^*} \langle \hat{H} \rangle - \chi_{\sigma \mathbf{k}}^2 \frac{\partial}{\partial \chi_{\sigma \mathbf{k}}} \langle \hat{H} \rangle, \quad (\text{C14})$$

where we have used Eq. (C8b). Substituting the expression of $\langle \hat{H} \rangle$ from Eq. (C7) into Eqs. (C10) and (C14) leads to

From this equation we then derive Eq. (C15) as an approximation to the exact Heisenberg quantum dynamics.

First, consider $\hat{O} = a_{\sigma \mathbf{k}=0}$. From Eq. (C17) one can show that

$$\begin{aligned} V(i\hbar) \frac{d}{dt} \Psi_{\sigma 0} &= i\hbar \sqrt{V} \frac{d}{dt} \langle a_{\sigma \mathbf{k}=0} \rangle \approx \sqrt{V} \langle [\hat{O}, \hat{H}] \rangle \\ &= \frac{\partial}{\partial \Psi_{\sigma 0}^*} \langle \hat{H} \rangle. \end{aligned} \quad (\text{C18})$$

Apart from the approximate sign, this equation is identical to Eq. (C10). Similarly, it follows that for the Cooper-like pairing field $\hat{O} = a_{\sigma \mathbf{k}} a_{\sigma -\mathbf{k}}$,

$$\begin{aligned} i\hbar \frac{d}{dt} x_{\mathbf{k}} &= i\hbar \frac{d}{dt} \langle a_{\sigma \mathbf{k}} a_{\sigma -\mathbf{k}} \rangle \approx \langle [\hat{O}, \hat{H}] \rangle \\ &= \frac{\partial}{\partial \chi_{\sigma \mathbf{k}}^*} \langle \hat{H} \rangle - \chi_{\sigma \mathbf{k}}^2 \frac{\partial}{\partial \chi_{\sigma \mathbf{k}}} \langle \hat{H} \rangle, \end{aligned} \quad (\text{C19})$$

which is essentially identical to Eq. (C12). The remaining derivations leading to Eq. (C15) are the same as in the previous section.

APPENDIX D: REGULARIZATION AND RENORMALIZATION

Because we have used contact interactions in the Hamiltonian Eq. (1) in the main text, solving Eq. (C15) requires a proper regularization to avoid ultraviolet divergences in integrals over \mathbf{k} . The regularizations can be determined by matching the equilibrium version of Eq. (C15) with the

corresponding Lippmann-Schwinger equation in the two-body scattering limit as done in Ref. [56].

For the open-channel atoms, a correct renormalization condition, that is compatible with the definition of \hat{H} in Eq. (1) of the main text, is given as follows [54]:

$$g_1 = \bar{g}_1 \Gamma, \quad (\text{D1a})$$

$$\alpha = \bar{\alpha} \Gamma / \sqrt{2}, \quad (\text{D1b})$$

$$\nu = \bar{\nu} + \sqrt{2} \beta \alpha \bar{\alpha}, \quad (\text{D1c})$$

with

$$\bar{g}_1 = \frac{4\pi \hbar^2 a_{\text{bg}}}{m_1}, \quad (\text{D2a})$$

$$\beta = \frac{m_1 \Lambda}{2\pi^2 \hbar^2}. \quad (\text{D2b})$$

$$\Gamma = \frac{1}{1 - \beta \bar{g}_1}, \quad (\text{D2c})$$

$$\bar{\alpha}^2 = \bar{g}_1 \Delta \mu_m \Delta B, \quad (\text{D2d})$$

$$\bar{\nu} = \Delta \mu_m (B - B_0). \quad (\text{D2e})$$

In these equations, quantities denoted with a bar atop represent the renormalized (or physical) ones that are directly related to experimental observables, while those without the bar are bare ones whose value depends on the cutoff Λ . a_{bg} is the atom-atom background scattering length. B is the applied external magnetic field in experiments, and B_0 corresponds to the resonance point where the atom-atom scattering length diverges. ΔB is the resonance width measured in magnetic fields, and $\Delta \mu_m$ is the magnetic moment difference between a pair of atoms in the open channel and a molecule in the closed channel.

One can also derive the regularization and renormalization relations in Eq. (D1) directly from Eq. (C15) by considering the zero-density limit of the latter. In this limit we ignore the dynamics of Ψ_{20} and $x_{1\mathbf{k}}$ in Eq. (C15), integrate them out, incorporate their effects into the equation for $i\hbar d\Psi_{10}/dt$, and cast the obtained results into a form of Gross-Pitaevskii equation for Ψ_{10} , with the following effective atom-atom interaction parameter:

$$g_{1,\text{eff}} = \frac{g_1}{1 + g_1 \beta} - \frac{2\alpha^2 / (1 + g_1 \beta)^2}{\nu - 2\beta \frac{\alpha^2}{1 + g_1 \beta}}. \quad (\text{D3})$$

This $g_{1,\text{eff}}$ is identified with $4\pi \hbar^2 a_s / m_1$, where a_s is the ν -dependent atom-atom scattering length. Comparing this result with the definition of a_s in terms of physical observables,

$$a_s \equiv a_{\text{bg}} - \frac{m_1}{4\pi \hbar^2} \frac{\bar{\alpha}^2}{\bar{\nu}} = a_{\text{bg}} \left(1 - \frac{\Delta B}{B - B_0} \right), \quad (\text{D4})$$

we immediately see that Eq. (D1) is a correct renormalization condition. In Eq. (D4), $\bar{\alpha}$ measures the Feshbach resonance width in units of energy, and $\bar{\nu} = \Delta \mu_m (B - B_0)$ is the detuning measured in energy.

For the closed-channel molecules, the proper regularization that connects the bare interaction parameter g_2 to the molecule-molecule background scattering length $a_{\text{mm,bg}}$ is

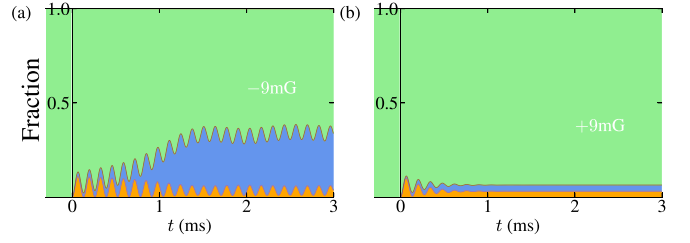


FIG. 6. Contrast between the quench dynamics at large negative [panel (a)] and positive [panel (b)] detuning. Shaded green, blue, and orange regimes represent the atomic condensate, noncondensed pair, and molecular condensate fraction, respectively. Indicated in white are the quenched detuning $\bar{\nu} / \Delta \mu_m = B - B_0$ (in mG).

given by the following Lippmann-Schwinger equation:

$$\frac{m_2}{4\pi \hbar^2 a_{\text{mm,bg}}} = \frac{1}{g_2} + \int^{\Lambda} \frac{d\mathbf{k}}{(2\pi)^3} \frac{1}{\hbar^2 \mathbf{k}^2 / m_2}, \quad (\text{D5})$$

where $m_2 = 2m_1$ is the molecule mass and $a_{\text{mm,bg}}$ is the molecule-molecule background scattering length. In principle, the cutoff Λ here can be different from the one used in Eq. (D1). Here, we take them to be the same.

From the experimental values of $\{a_{\text{bg}}, \Delta \mu_m, \Delta B\}$ from Table I and $a_{\text{mm,bg}} = 220a_B$, taken from Refs. [7,8], we determine the bare interaction parameters $\{\alpha, g_1, g_2\}$ in our Hamiltonian for a chosen cutoff Λ , using the renormalization conditions in Eqs. (D1) and (D5). In our numerics we leave the cutoff Λ as a relatively free parameter, which is adjusted such that the resulting results are in reasonable agreement with the experiments at comparable detuning. In Table II we list the parameters $\{g_1, g_2, \alpha, \Lambda\}$ that we have used in our simulations.

APPENDIX E: UNDERSTANDING THE PAIRING CONTRIBUTIONS

In this section we give a more extensive discussion of the pairing contributions that appear after a quench of an atomic condensate as the quenched detuning is varied towards resonance and even beyond. It is shown here that this introduction of the pairs which occurs during the transient stage essentially instigates the subsequent dynamics.

There seem to be two schools of thought on the atom-molecule dynamics. In the first of these all dynamical processes and oscillations are associated with the condensates only [20] (although fluctuation effects can also be contemplated), whereas in the second [43,54] pairing contributions are important, although they have not been treated before in the presence of a substantial fraction of closed-channel superfluid molecules. It should be clear here that our approach is to be distinguished from the condensates-only scheme. Notably, in Ref. [8] such an approach was taken but in the context of an extended three-body interaction term. One can, in fact, make a case that the three-body Hamiltonian introduced in Ref. [8] will be in some sense an effective interaction between condensed atom and molecules, mediated by pairs through higher-order (in Feshbach coupling) contributions of the latter.

We begin with Fig. 6(a), which addresses a sweep from an atomic condensate to somewhat further to the molecular side of resonance than in Fig. 2(a) in the main text. It is worth concentrating on the detailed time dependence, as this shows

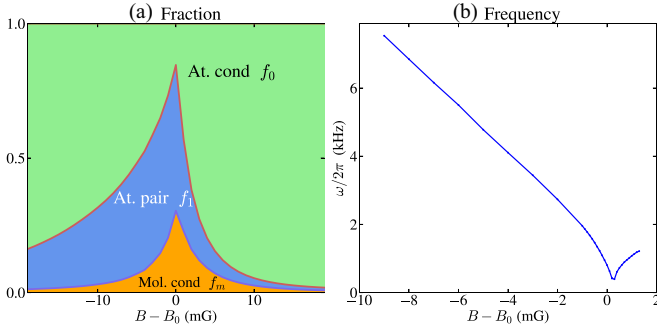


FIG. 7. Panel (a) shows the time-averaged weight of each of the three components (atomic condensate fraction $f_0 = |\Psi_{10}|^2/n$, non-condensed atom-pair fraction $f_1 = n_1/n$, and molecule fraction $f_m = 2|\Psi_{20}|^2/n$) as a function of the quenched detuning $\bar{\nu}/\Delta\mu_m = B - B_0$. The results are obtained for the steady state reached after a quench as in Figs. 3(a) and 3(b) in the main text. It relates to Fig. 4(a) in the main text by showing the quantities that were not plotted in Fig. 4(a), namely, f_0 and f_1 ; the results here could serve as a good basis for predictions to be addressed experimentally in the future. (b) This figure plots the steady-state oscillation frequency ω as a function of the quenched detuning $B - B_0$ for fixed particle number density $n = 2.9 \times 10^{13} \text{ cm}^{-3}$.

that in the early stages of the evolution the greatest change is associated with the creation of a molecular condensate. But shortly thereafter the pairing contribution begins to grow. In this case an overall envelope shows that the pairing is growing at the expense of the atomic condensate, and this is expected because this sweep is deeper on the molecular side so that the initial atomic condensate is less stable. After a transient, the molecular condensate is frozen and rather time independent, except for small oscillations. In addition, there is a three-way coupled oscillation between the atomic and the molecular condensates and the pairs.

If we compare Fig. 6(a) with 6(b), where the final state of the system is on the atomic side of resonance, it is clear that the molecular condensate and the pairing terms are in this new figure much reduced in magnitude. In Fig. 6(b), one sees that the atomic condensate is not as driven to decay, since it is not as unstable as in the previous case. Hence we see fewer pairs. Here, too, one sees after a transient that there is a three-way coupled oscillation.

We next turn to the component contributions for more general situations where the final-state detuning is varied continuously. This is plotted in Fig. 7(a). This figure can be compared to Fig. 4(a) in the main text. What is most striking here is that while the molecular boson contributions are reasonably symmetric around resonance, the pair contribution is more significant on the molecular side, as already seen in Fig. 6. Indeed, we have argued in the text for such an asymmetry based on energy conservation issues. When the molecular level is far below the atomic level, the creation of molecules must be compensated by introducing higher-energy states, in this case pairs.

In addition to this asymmetry, what is rather interesting here is that there is a re-stabilization of the atomic condensate deep into the molecular side of resonance. This is rather similar to what one would observe in a simple two-level Rabi oscillation.

For completeness, we also show in Fig. 7(b) the steady-state oscillation frequency vs detuning $B - B_0$. There is a clear V shape, with a minimum of frequency at $B - B_0$ very close to zero, corresponding to the two-body resonance, but more precisely at $B - B_0 \approx 0.25 \text{ mG}$. Here the plot terminates at $B - B_0 = 2 \text{ mG}$, because the oscillations above 2 mG are completely damped.

In summary, given that there is a dichotomy between pairing contributions and condensate-only contributions (but which go beyond the simple two-body Feshbach coupling), it will be important in the future to obtain more direct experimental evidence for or against these noncondensed pair effects. Similarly, for future theory it may be important to include direct pairwise intercondensate correlations.

APPENDIX F: MORE DETAILS ON THEORY-EXPERIMENT COMPARISON: DEPENDENCE OF THE OSCILLATION FREQUENCY ON THE PARTICLE DENSITY

It is important to point out that the experimental data in Fig. 4(b) are collected for $B - B_0 = -1 \text{ mG}$, which is not strictly at unitarity where the theory was addressed. There is some experimental uncertainty ($\sim 2 \text{ mG}$) in the measured B field, which mainly comes from environmentally caused stray fields (of about 14 mG). We suppress the stray magnetic fields by a servo loop to the level of 2 mG.

Given this uncertainty, if we use our theoretical result at $B - B_0 = -1 \text{ mG}$ to compare with the experiment, as shown in Fig. 8, we see that the oscillation frequency magnitude is actually in rather good agreement with the experimental data.

Importantly, in the context of Fig. 8, while there is a discrepancy in the power-law exponent between theory and experiment, we argue that this does not mean there is a contradiction between the theoretical model description used in the current paper and the three-body recombination mechanism advocated in Ref. [8]. Even though the microscopic two-channel Hamiltonian we started with only contains Feshbach coupling (α) and pairwise density-density interactions (g_1 and g_2), it can induce three-body recombination through scattering processes that are higher order than linear in α . This should not be surprising, since the two-channel Hamiltonian (with point contact interactions) has been used in the literature to discuss three-body recombination and related Efimov physics. See Ref. [48], for example. The two- and three-body model Hamiltonians used in Ref. [8] should be understood as the *full two- and three-body scattering amplitudes* between atom and molecules derived from an infinite sum of microscopic scattering processes resulting from the two-channel microscopic Hamiltonian.

APPENDIX G: POSSIBLE CAUSES OF THE DISCREPANCY BETWEEN THE THEORY AND EXPERIMENT IN THE MINIMAL OSCILLATION FREQUENCY

The comparison between our theory and experiment is not perfect. In particular, there is a discrepancy in the minimal oscillation frequency as a function of detuning between the experimental results and theory (see Fig. 7 and Fig. 3(d) of Ref. [8]). One may speculate that some of the following

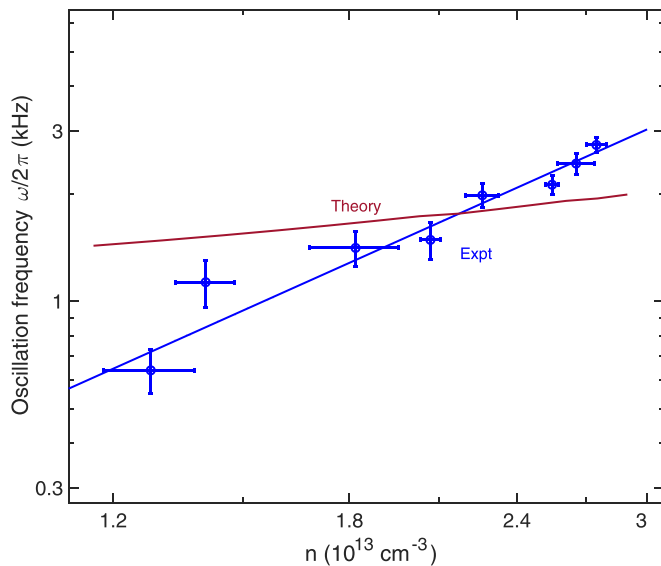


FIG. 8. Density (n) dependence of the oscillation frequency (ω) near unitarity. The experimental data are the same as in Fig. 4(b) of the main text. The theoretical curve, in magenta, is taken at $B - B_0 = -1$ mG, which should be contrasted with the theoretical curve in Fig. 4(b) of the main text, which is for $B - B_0 = 0$ mG. The theoretical curve at $B - B_0 = -1$ mG here roughly follows $\omega \propto n^{0.6}$ within the density range plotted. The comparison here is to show that if one takes into account the fact that the experimental data is collected for $B - B_0 = -1$ mG, a much better agreement between the magnitude of the theoretical and experimental oscillation frequencies can be obtained.

points, which are largely ignored in the theoretical literature as well as in the current theoretical treatment, have contributed to this discrepancy:

(1) In our theoretical modeling we have ignored a possible interchannel density-density interaction term, $g_{12} \sum_{\mathbf{k}_1, \mathbf{k}_2, \mathbf{k}_3} a_{1, \mathbf{k}_1}^\dagger a_{1, \mathbf{k}_2} a_{2, \mathbf{k}_3}^\dagger a_{2, \mathbf{k}_1 + \mathbf{k}_3 - \mathbf{k}_2}$, which will make additional contributions to the dynamic equations of both atom and molecule condensates, $d\Psi_{10}/dt$ and $d\Psi_{20}/dt$, if we assume that the g_{12} effect is elastic. This additional term depends on the amplitudes of both atom and molecule condensates, $|\Psi_{10}|$ and $|\Psi_{20}|$. Given that this term is off-diagonal in the subspace spanned by the atom and molecule condensate energy levels, it behaves very much like the interlevel coupling term in a two-level Rabi oscillation problem; therefore, one expects that including this term will lead to a larger minimal oscillation frequency. The existence of this contribution, which is proportional to $|\Psi_{10}|$ and $|\Psi_{20}|$, is also consistent with the observation that the minimal oscillation frequency in Fig. 3(d) of Ref. [8] increases with the initial atom BEC fraction.

(2) Another simplification which we make and which is widespread in the literature is to drop correlations, such as $\langle a_{1, \mathbf{k}} a_{2, -\mathbf{k}} \rangle$, in our many-body trial wave function. Including these additional interchannel correlations, which increases the complexity significantly, can also affect the minimal oscillation frequency.

(3) Lastly, in our theoretical modeling we have ignored various possible loss processes due to atom-atom and atom-molecule inelastic collision.

- [1] J. L. Bohn, A. M. Rey, and J. Ye, Cold molecules: Progress in quantum engineering of chemistry and quantum matter, *Science* **357**, 1002 (2017).
- [2] L. D. Carr, D. DeMille, R. V. Krems, and J. Ye, Cold and ultracold molecules: Science, technology and applications, *New J. Phys.* **11**, 055049 (2009).
- [3] G. Quemener and P. S. Julienne, Ultracold molecules under control! *Chem. Rev.* **112**, 4949 (2012).
- [4] T. Langen, G. Valtolina, D. Wang, and J. Ye, Quantum state manipulation and cooling of ultracold molecules, *Nat. Phys.* **20**, 702 (2024).
- [5] L. De Marco, G. Valtolina, K. Matsuda, W. G. Tobias, J. P. Covey, and J. Ye, A degenerate Fermi gas of polar molecules, *Science* **363**, 853 (2019).
- [6] S. Jochim, M. Bartenstein, A. Altmeyer, G. Hendl, S. Riedl, C. Chin, J. Hecker Denschlag, and R. Grimm, Bose-Einstein condensation of molecules, *Science* **302**, 2101 (2003).
- [7] Z. Zhang, L. Chen, K.-X. Yao, and C. Chin, Transition from an atomic to a molecular Bose-Einstein condensate, *Nature (London)* **592**, 708 (2021).
- [8] Z. Zhang, S. Nagata, K. Yao, and C. Chin, Many-body chemical reactions in a quantum degenerate gas, *Nat. Phys.* **19**, 1466 (2023).
- [9] C. Chin, R. Grimm, P. Julienne, and E. Tiesinga, Feshbach resonances in ultracold gases, *Rev. Mod. Phys.* **82**, 1225 (2010).
- [10] S. E. Pollack, D. Dries, M. Junker, Y. P. Chen, T. A. Corcovilos, and R. G. Hulet, Extreme tunability of interactions in a ^7Li Bose-Einstein condensate, *Phys. Rev. Lett.* **102**, 090402 (2009).
- [11] E. A. Donley, N. R. Claussen, S. T. Thompson, and C. E. Wieman, Atom-molecule coherence in a Bose-Einstein condensate, *Nature (London)* **417**, 529 (2002).
- [12] M. Holland, S. J. J. M. F. Kokkelmans, M. L. Chiofalo, and R. Walser, Resonance superfluidity in a quantum degenerate Fermi gas, *Phys. Rev. Lett.* **87**, 120406 (2001).
- [13] C. Eigen, J. A. P. Glidden, R. Lopes, E. A. Cornell, R. P. Smith, and Z. Hadzibabic, Universal prethermal dynamics of Bose gases quenched to unitarity, *Nature (London)* **563**, 221 (2018).
- [14] C. D'Errico, M. Zaccanti, M. Fattori, G. Roati, M. Inguscio, G. Modugno, and A. Simoni, Feshbach resonances in ultracold ^{39}K , *New J. Phys.* **9**, 223 (2007).
- [15] T.-L. Ho, X. Cui, and W. Li, Alternative route to strong interaction: Narrow Feshbach resonance, *Phys. Rev. Lett.* **108**, 250401 (2012).
- [16] L. Radzihovsky, J. Park, and P. B. Weichman, Superfluid transitions in bosonic atom-molecule mixtures near a Feshbach resonance, *Phys. Rev. Lett.* **92**, 160402 (2004).
- [17] M. W. J. Romans, R. A. Duine, S. Sachdev, and H. T. C. Stoof, Quantum phase transition in an atomic Bose gas with a Feshbach resonance, *Phys. Rev. Lett.* **93**, 020405 (2004).

- [18] D. M. Stamper-Kurn, A. P. Chikkatur, A. Görlitz, S. Inouye, S. Gupta, D. E. Pritchard, and W. Ketterle, Excitation of phonons in a Bose-Einstein condensate by light scattering, *Phys. Rev. Lett.* **83**, 2876 (1999).
- [19] D. J. Heinzen, R. Wynar, P. D. Drummond, and K. V. Kheruntsyan, Superchemistry: Dynamics of coupled atomic and molecular Bose-Einstein condensates, *Phys. Rev. Lett.* **84**, 5029 (2000).
- [20] A. Vardi, V. A. Yurovsky, and J. R. Anglin, Quantum effects on the dynamics of a two-mode atom-molecule Bose-Einstein condensate, *Phys. Rev. A* **64**, 063611 (2001).
- [21] F. Richter, D. Becker, C. Beny, T. A. Schulze, S. Ospelkaus, and T. J. Osborne, Ultracold chemistry and its reaction kinetics, *New J. Phys.* **17**, 055005 (2015).
- [22] N. R. Claussen, E. A. Donley, S. T. Thompson, and C. E. Wieman, Microscopic dynamics in a strongly interacting Bose-Einstein condensate, *Phys. Rev. Lett.* **89**, 010401 (2002).
- [23] P. Makotyn, C. E. Klauss, D. L. Goldberger, E. A. Cornell, and D. S. Jin, Universal dynamics of a degenerate unitary Bose gas, *Nat. Phys.* **10**, 116 (2014).
- [24] C. Eigen, J. A. P. Glidden, R. Lopes, N. Navon, Z. Hadzibabic, and R. P. Smith, Universal scaling laws in the dynamics of a homogeneous unitary Bose gas, *Phys. Rev. Lett.* **119**, 250404 (2017).
- [25] A. Koetsier, P. Massignan, R. A. Duine, and H. T. C. Stoof, Strongly interacting Bose gas: Nozières and Schmitt-Rink theory and beyond, *Phys. Rev. A* **79**, 063609 (2009).
- [26] G. S. Jeon, L. Yin, S. W. Rhee, and D. J. Thouless, Pairing instability and mechanical collapse of a Bose gas with an attractive interaction, *Phys. Rev. A* **66**, 011603(R) (2002).
- [27] E. J. Mueller and G. Baym, Finite-temperature collapse of a Bose gas with attractive interactions, *Phys. Rev. A* **62**, 053605 (2000).
- [28] S. Basu and E. J. Mueller, Stability of bosonic atomic and molecular condensates near a Feshbach resonance, *Phys. Rev. A* **78**, 053603 (2008).
- [29] A. D. Lange, K. Pilch, A. Prantner, F. Ferlaino, B. Engeser, H.-C. Nägerl, R. Grimm, and C. Chin, Determination of atomic scattering lengths from measurements of molecular binding energies near Feshbach resonances, *Phys. Rev. A* **79**, 013622 (2009).
- [30] See the Appendices for details on the experiment, the quantification of Feshbach resonance width, the derivation of Eq. (2), the regularization conditions used for the interaction parameters in the Hamiltonian \hat{H} , and further discussions on the pairing contribution to the postquench dynamics as well as on the theory-experiment comparison.
- [31] S. S. Natu and E. J. Mueller, Dynamics of correlations in a dilute Bose gas following an interaction quench, *Phys. Rev. A* **87**, 053607 (2013).
- [32] A. Rancon, C.-L. Hung, C. Chin, and K. Levin, Quench dynamics in Bose-Einstein condensates in the presence of a bath: Theory and experiment, *Phys. Rev. A* **88**, 031601(R) (2013).
- [33] B. Kain and H. Y. Ling, Nonequilibrium states of a quenched Bose gas, *Phys. Rev. A* **90**, 063626 (2014).
- [34] A. G. Sykes, J. P. Corson, J. P. D’Incao, A. P. Koller, C. H. Greene, A. M. Rey, K. R. A. Hazzard, and J. L. Bohn, Quenching to unitarity: Quantum dynamics in a three-dimensional Bose gas, *Phys. Rev. A* **89**, 021601(R) (2014).
- [35] J. P. Corson and J. L. Bohn, Bound-state signatures in quenched Bose-Einstein condensates, *Phys. Rev. A* **91**, 013616 (2015).
- [36] G. Menegoz and A. Silva, Prethermalization of weakly interacting bosons after a sudden interaction quench, *J. Stat. Mech.* (2015) P05035.
- [37] X. Yin and L. Radzihovsky, Postquench dynamics and prethermalization in a resonant Bose gas, *Phys. Rev. A* **93**, 033653 (2016).
- [38] M. Van Regemortel, H. Kurkjian, M. Wouters, and I. Carusotto, Prethermalization to thermalization crossover in a dilute Bose gas following an interaction ramp, *Phys. Rev. A* **98**, 053612 (2018).
- [39] A. Munoz de las Heras, M. M. Parish, and F. M. Marchetti, Early-time dynamics of Bose gases quenched into the strongly interacting regime, *Phys. Rev. A* **99**, 023623 (2019).
- [40] J. Haegeman, J. I. Cirac, T. J. Osborne, I. Pižorn, H. Verschelde, and F. Verstraete, Time-dependent variational principle for quantum lattices, *Phys. Rev. Lett.* **107**, 070601 (2011).
- [41] T. Shi, E. Demler, and J. Ignacio Cirac, Variational study of fermionic and bosonic systems with non-Gaussian states: Theory and applications, *Ann. Phys.* **390**, 245 (2018).
- [42] P. Kramer, A review of the time-dependent variational principle, *J. Phys. Conf. Ser.* **99**, 012009 (2008).
- [43] M. Holland, J. Park, and R. Walser, Formation of pairing fields in resonantly coupled atomic and molecular Bose-Einstein condensates, *Phys. Rev. Lett.* **86**, 1915 (2001).
- [44] Z. Wang, K. Wang, Q. J. Chen, C. Chin, and K. Levin, Molecular condensates of atomic Bose gases: stability considerations (working title, unpublished).
- [45] In the experiments the fraction plotted is for both condensed and noncondensed closed-channel molecules, whereas in theory almost all closed-channel molecules are condensed.
- [46] M. Mark, T. Kraemer, J. Herbig, C. Chin, H.-C. Nägerl, and R. Grimm, Efficient creation of molecules from a cesium Bose-Einstein condensate, *Europhys. Lett.* **69**, 706 (2005).
- [47] T. Köhler, K. Góral, and P. S. Julienne, Production of cold molecules via magnetically tunable Feshbach resonances, *Rev. Mod. Phys.* **78**, 1311 (2006).
- [48] P. F. Bedaque, E. Braaten, and H.-W. Hammer, Three-body recombination in Bose gases with large scattering length, *Phys. Rev. Lett.* **85**, 908 (2000).
- [49] A. Tenart, G. Hercé, J.-P. Bureik, A. Dareaux, and D. Clément, Observation of pairs of atoms at opposite momenta in an equilibrium interacting Bose gas, *Nat. Phys.* **17**, 1364 (2021).
- [50] L. W. Clark, A. Gaj, L. Feng, and C. Chin, Collective emission of matter-wave jets from driven Bose-Einstein condensates, *Nature (London)* **551**, 356 (2017).
- [51] K. Xu, T. Mukaiyama, J. R. Abo-Shaeer, J. K. Chin, D. E. Miller, and W. Ketterle, Formation of quantum-degenerate sodium molecules, *Phys. Rev. Lett.* **91**, 210402 (2003).
- [52] S. Dürr, T. Volz, A. Marte, and G. Rempe, Observation of molecules produced from a Bose-Einstein condensate, *Phys. Rev. Lett.* **92**, 020406 (2004).

- [53] A. Frisch, M. Mark, K. Aikawa, S. Baier, R. Grimm, A. Petrov, S. Kotochigova, G. Quéméner, M. Lepers, O. Dulieu, and F. Ferlaino, Ultracold dipolar molecules composed of strongly magnetic atoms, *Phys. Rev. Lett.* **115**, 203201 (2015).
- [54] S. J. J. M. F. Kokkelmans and M. J. Holland, Ramsey fringes in a Bose-Einstein condensate between atoms and molecules, *Phys. Rev. Lett.* **89**, 180401 (2002).
- [55] T. Köhler, T. Gasenzer, and K. Burnett, Microscopic theory of atom-molecule oscillations in a Bose-Einstein condensate, *Phys. Rev. A* **67**, 013601 (2003).
- [56] S. J. J. M. F. Kokkelmans, J. N. Milstein, M. L. Chiofalo, R. Walser, and M. J. Holland, Resonance superfluidity: Renormalization of resonance scattering theory, *Phys. Rev. A* **65**, 053617 (2002).